

# Studying different illumination patterns for resolution improvement in fluorescence microscopy

Nadya Chakrova,<sup>1</sup> Rainer Heintzmann,<sup>2,3</sup> Bernd Rieger,<sup>1</sup> and Sjoerd Stallinga<sup>1,\*</sup>

<sup>1</sup>Imaging Physics Department, Delft University of Technology, Lorentzweg 1, 2628CJ Delft, The Netherlands

<sup>2</sup>Leibniz Institute of Photonic Technology, Albert-Einstein Str. 9, 07745 Jena, Germany

<sup>3</sup>Institute of Physical Chemistry, Friedrich-Schiller University Jena, Helmholtzweg 4, 07743 Jena, Germany  
[s.stallinga@tudelft.nl](mailto:s.stallinga@tudelft.nl)

**Abstract:** Various types of non-uniform illumination can be used for resolution improvement in fluorescence microscopy. Here we study the differences between several types of incoherent illumination patterns, such as multi-spot, line and pseudo-random patterns. This requires an imaging setup and an image reconstruction algorithm that are flexible enough to incorporate any type of illumination pattern. We employ fluorescence microscope with structured illumination generated by a Digital Micro-mirror Device (DMD) and the pattern-illuminated Fourier Ptychography reconstruction algorithm (piFP) to this end. The piFP method is modified and improved by identifying the algorithm as steepest descent optimization of a least squares function. We find that illumination patterns with regular structure are superior to those with irregular structure in terms of resolution enhancement and noise level in the reconstructed images.

©2015 Optical Society of America

**OCIS codes:** (180.2520) Fluorescence microscopy; (100.6640) Superresolution; (100.3190) Inverse problems.

---

## References and links

1. M. G. Gustafsson, "Surpassing the lateral resolution limit by a factor of two using structured illumination microscopy," *J. Microsc.* **198**(2), 82–87 (2000).
2. R. Heintzmann and C. Cremer, "Laterally modulated excitation microscopy: improvement of resolution by using a diffraction grating," *Proc. SPIE* **3568**, 185–196 (1999).
3. G. E. Cragg and P. T. So, "Lateral resolution enhancement with standing evanescent waves," *Opt. Lett.* **25**(1), 46–48 (2000).
4. J. T. Frohn, H. F. Knapp, and A. Stemmer, "True optical resolution beyond the Rayleigh limit achieved by standing wave illumination," *Proc. Natl. Acad. Sci. U.S.A.* **97**(13), 7232–7236 (2000).
5. M. G. L. Gustafsson, L. Shao, P. M. Carlton, C. J. R. Wang, I. N. Golubovskaya, W. Z. Cande, D. A. Agard, and J. W. Sedat, "Three-dimensional resolution doubling in wide-field fluorescence microscopy by structured illumination," *Biophys. J.* **94**(12), 4957–4970 (2008).
6. L. Shao, P. Kner, E. H. Rego, and M. G. L. Gustafsson, "Super-resolution 3D microscopy of live whole cells using structured illumination," *Nat. Methods* **8**(12), 1044–1046 (2011).
7. S. W. Hell and J. Wichmann, "Breaking the diffraction resolution limit by stimulated emission: stimulated-emission-depletion fluorescence microscopy," *Opt. Lett.* **19**(11), 780–782 (1994).
8. E. Betzig, G. H. Patterson, R. Sougrat, O. W. Lindwasser, S. Olenych, J. S. Bonifacino, M. W. Davidson, J. Lippincott-Schwartz, and H. F. Hess, "Imaging intracellular fluorescent proteins at nanometer resolution," *Science* **313**(5793), 1642–1645 (2006).
9. M. J. Rust, M. Bates, and X. Zhuang, "Sub-diffraction-limit imaging by stochastic optical reconstruction microscopy (STORM)," *Nat. Methods* **3**(10), 793–796 (2006).
10. S. T. Hess, T. P. K. Girirajan, and M. D. Mason, "Ultra-high resolution imaging by fluorescence photoactivation localization microscopy," *Biophys. J.* **91**(11), 4258–4272 (2006).
11. D. Li, L. Shao, B.-C. Chen, X. Zhang, M. Zhang, B. Moses, D. E. Milkie, J. R. Beach, J. A. Hammer 3rd, M. Pasham, T. Kirchhausen, M. A. Baird, M. W. Davidson, P. Xu, and E. Betzig, "Extended-resolution structured illumination imaging of endocytic and cytoskeletal dynamics," *Science* **349**(6251), aab3500 (2015).
12. K. Wicker, "Non-iterative determination of pattern phase in structured illumination microscopy using auto-correlations in Fourier space," *Opt. Express* **21**(21), 24692–24701 (2013).
13. K. Wicker, O. Mandula, G. Best, R. Fiolka, and R. Heintzmann, "Phase optimisation for structured illumination microscopy," *Opt. Express* **21**(2), 2032–2049 (2013).

14. E. Mudry, K. Belkebir, J. Girard, J. Savatier, E. Le Moal, C. Nicoletti, M. Allain, and A. Sentenac, "Structured illumination microscopy using unknown speckle patterns," *Nat. Photonics* **6**(5), 312–315 (2012).
15. R. Ayuk, H. Giovannini, A. Jost, E. Mudry, J. Girard, T. Mangeat, N. Sandeau, R. Heintzmann, K. Wicker, K. Belkebir, and A. Sentenac, "Structured illumination fluorescence microscopy with distorted excitations using a filtered blind-SIM algorithm," *Opt. Lett.* **38**(22), 4723–4726 (2013).
16. J. Min, J. Jang, D. Keum, S.-W. Ryu, C. Choi, K.-H. Jeong, and J. C. Ye, "Fluorescent microscopy beyond diffraction limits using speckle illumination and joint support recovery," *Sci. Rep.* **3**, 2075 (2013).
17. A. Jost, E. Tolstik, P. Feldmann, K. Wicker, A. Sentenac, and R. Heintzmann, "Optical sectioning and high resolution in single-slice Structured Illumination Microscopy by thick slice blind-SIM reconstruction," *PLoS One* **10**(7), e0132174 (2015).
18. S. Dong, P. Nanda, R. Shiradkar, K. Guo, and G. Zheng, "High-resolution fluorescence imaging via pattern-illuminated Fourier ptychography," *Opt. Express* **22**(17), 20856–20870 (2014).
19. G. Zheng, R. Horstmeyer, and C. Yang, "Wide-field, high-resolution Fourier ptychographic microscopy," *Nat. Photonics* **7**(9), 739–745 (2013).
20. M. G. Somekh, C. W. See, and J. Goh, "Wide field amplitude and phase confocal microscope with speckle illumination," *Opt. Commun.* **174**(1-4), 75–80 (2000).
21. C. Ventalon and J. Mertz, "Quasi-confocal fluorescence sectioning with dynamic speckle illumination," *Opt. Lett.* **30**(24), 3350–3352 (2005).
22. J. G. Walker, "Non-scanning confocal fluorescence microscopy using speckle illumination," *Opt. Commun.* **189**(4-6), 221–226 (2001).
23. M. Liang, R. L. Stehr, and A. W. Krause, "Confocal pattern period in multiple-aperture confocal imaging systems with coherent illumination," *Opt. Lett.* **22**(11), 751–753 (1997).
24. Q. S. Hanley, P. J. Verveer, M. J. Gemkow, D. Arndt-Jovin, and T. M. Jovin, "An optical sectioning programmable array microscope implemented with a digital micromirror device," *J. Microsc.* **196**(3), 317–331 (1999).
25. R. Heintzmann, Q. S. Hanley, D. Arndt-Jovin, and T. M. Jovin, "A dual path programmable array microscope (PAM): simultaneous acquisition of conjugate and non-conjugate images," *J. Microsc.* **204**(2), 119–135 (2001).
26. P. J. Verveer, Q. S. Hanley, P. W. Verbeek, L. J. v Vliet, and T. M. Jovin, "Theory of confocal fluorescence imaging in the programmable array microscope (PAM)," *J. Microsc.* **189**(3), 192–198 (1998).
27. P. Křížek, I. Raška, and G. M. Hagen, "Flexible structured illumination microscope with a programmable illumination array," *Opt. Express* **20**(22), 24585–24599 (2012).
28. A. G. York, S. H. Parekh, D. D. Nogare, R. S. Fischer, K. Temprine, M. Mione, A. B. Chitnis, C. A. Combs, and H. Shroff, "Resolution doubling in live, multicellular organisms via multifocal structured illumination microscopy," *Nat. Methods* **9**(7), 749–754 (2012).
29. D. Dan, M. Lei, B. Yao, W. Wang, M. Winterhalder, A. Zumbusch, Y. Qi, L. Xia, S. Yan, Y. Yang, P. Gao, T. Ye, and W. Zhao, "DMD-based LED-illumination Super-resolution and optical sectioning microscopy," *Sci. Rep.* **3**, 1116 (2013).
30. M. Guizar-Sicairos and J. R. Fienup, "Phase retrieval with transverse translation diversity: a nonlinear optimization approach," *Opt. Express* **16**(10), 7264–7278 (2008).
31. C. L. Luengo Hendriks, B. Rieger, M. van Ginkel, G. M. P. van Kempen, and L. J. van Vliet, "DIPimage: a scientific image processing toolbox for MATLAB," Delft University of Technology (1999).
32. S. A. Shroff, J. R. Fienup, and D. R. Williams, "Phase-shift estimation in sinusoidally illuminated images for lateral superresolution," *J. Opt. Soc. Am. A* **26**(2), 413–424 (2009).
33. N. Chakrova, B. Rieger, and S. Stallinga, "Development of a DMD-based fluorescence microscope," *Proc. SPIE* **9330**, 933008 (2015).
34. C. H. Righolt, J. A. Slotman, I. T. Young, S. Mai, L. J. van Vliet, and S. Stallinga, "Image filtering in structured illumination microscopy using the Lukosz bound," *Opt. Express* **21**(21), 24431–24451 (2013).
35. M. Ingaramo, A. G. York, E. Hoogendoorn, M. Postma, H. Shroff, and G. H. Patterson, "Richardson-Lucy Deconvolution as a General Tool for Combining Images with Complementary Strengths," *ChemPhysChem* **15**(4), 794–800 (2014).
36. F. Ströhl and C. F. Kaminski, "A joint Richardson–Lucy deconvolution algorithm for the reconstruction of multifocal structured illumination microscopy data," *Methods Appl. Fluoresc.* **3**(1), 014002 (2015).

## 1. Introduction

Structured illumination microscopy (SIM) can be used to improve lateral resolution and optical sectioning capabilities of a fluorescence microscope. In standard wide-field fluorescence microscopy the sample is illuminated uniformly and the resolution is limited by diffraction to typically 180–250 nm laterally and 500–700 nm axially. In contrast to wide-field microscopy, in structured illumination microscopy multiple non-uniform illuminations are combined to improve sectioning and lateral resolution.

The mechanism responsible for the resolution improvement in structured illumination microscopy can be understood by considering the spatial frequency distributions of the illumination pattern and the sample. Multiplication of the sample structure with the illumination pattern in the object domain is equivalent to a convolution of the sample

spectrum with the illumination pattern spectrum in the Fourier domain. As a result of this convolution, sample frequencies beyond the diffraction limit are shifted into the detection passband of the microscope objective. As the excitation and emission passbands are equal in an epi-illumination setup up to a small correction due to the Stokes shift, a maximum resolution improvement by a factor of two can be reached.

In conventional SIM periodic line patterns, which are created by the interference of two or three parallel beams in the sample plane, are used to double the resolution. The final image is reconstructed from several images acquired at different positions and orientations of the line pattern. SIM has been implemented in various configurations [1–4] and has also been extended to 3D imaging [5] and live cell imaging [6]. Although several other super-resolution methods lead to a larger resolution improvement [7–10], SIM plays an increasingly important role in biological imaging due to its compatibility with live cell imaging and with the wide range of existing standard fluorescent dyes [11].

Image reconstruction in SIM requires an accurate knowledge of the shift between line pattern illuminations [12,13], and thus, is sensitive to misalignments and distortions of the illumination pattern. In order to lower the requirements on the precise knowledge of the illumination pattern in the reconstruction process, structured illumination methods with speckle illumination patterns have been developed. In the so-called blind-SIM approach unknown illumination patterns are reconstructed alongside the sample using a conjugate gradient algorithm [14,15] or other algorithm [16]. The recent advancements in blind-SIM methods allow processing of 2D slices acquired in thick samples [17]. These methods can use speckle patterns created by projecting the light transmitted by a diffuser onto the sample. This arrangement significantly simplifies the optical setup and lowers the requirements on the knowledge of the projected patterns. Moreover, the algorithms can be helpful in reconstructing images in classical SIM in case the illumination patterns are distorted. Nevertheless, the high computational demands of these methods may hamper their use in practice. A different, less computationally demanding technique to improve the resolution based on the speckle illumination was recently demonstrated by Zheng et al. [18]. The sample structure and shifted illumination speckle pattern are reconstructed using the pattern-illuminated Fourier Ptychography (piFP) algorithm, which is a Fourier Ptychography concept [19], modified for use in fluorescence microscopy. It is worth noting that besides the attempts to improve the lateral resolution, speckle illumination has also been applied in order to achieve optical sectioning in fluorescence microscopy [20–22]. Based on these studies the question arises whether SIM with regular illumination patterns (lines, spot arrays) or with irregular illumination patterns (speckle) is superior in terms of image quality.

In this paper we address this question using a flexible fluorescence microscope with structured illumination generated by a digital-micro-mirror device (DMD). The DMD-based fluorescence microscope belongs to the family of fluorescence microscopes with spatial light modulators integrated in their optical path [23–29]. We use the so-called single-pass configuration, where the DMD is placed only in the illumination path and the detection is standard widefield. The flexibility of the DMD allows us to study SIM with various types of illumination patterns, such as multi-spot, line, and pseudo-random patterns. An integral part of the imaging system is the reconstruction algorithm. We use the piFP technique, which can be used for any type of illumination pattern, thus matching the flexibility of our imaging setup. We start our treatment of image reconstruction for structured illumination microscopy by linking the piFP algorithm to steepest descent optimization of a quadratic function. Next, we investigate how the convergence speed of the piFP algorithm may be improved by modifying the iterative update step size. We then test the performance of different illumination patterns in terms of noise enhancement and resolution improvement. Finally, we demonstrate the differences in the behaviour of the various illumination patterns on bead samples and fixed biological samples.

## 2. Theory

### 2.1 Fourier Ptychography method as steepest descent of a quadratic function

In this section we will draw parallels between the iterative piFP scheme and least squares optimization via the steepest descent method. We consider an object represented by  $M$  pixels with intensities  $x_i$  ( $i = 1, 2, \dots, M$ ) that is illuminated by a set of  $N$  illumination patterns  $p_i^n$  ( $n = 1, 2, \dots, N$ ). Notice that here we model the continuous object as a discretized set of points, which is expected to give rise to correct results provided the sampling density is sufficiently high, i.e. above Nyquist. The expected photon count for pixel  $i$  and image  $n$  is given by the convolution sum:

$$\mu^n(\vec{r}_i) = \sum_{j=1}^M h^{em}(\vec{r}_i - \vec{r}_j) x(\vec{r}_j) p^n(\vec{r}_j), \quad (1)$$

where  $h^{em}(\vec{r})$  is the normalized emission point spread function (PSF) of the microscope. In the following we will use the shorthands  $h_{ij}^{em} = h^{em}(\vec{r}_i - \vec{r}_j)$ ,  $\mu_i^n = \mu^n(\vec{r}_i)$ ,  $x_i = x(\vec{r}_i)$ , and  $p_j^n = p^n(\vec{r}_j)$  for conciseness. The illumination patterns at the sample plane  $p_i^n$  are obtained from the DMD patterns  $q_i^n$  by convolution with the excitation PSF  $h^{ex}(\vec{r})$ :

$$p_i^n = \sum_{j=1}^M h_{ij}^{ex} q_j^n. \quad (2)$$

Here, effects of partial coherence in the illumination are neglected. The actually measured images  $d_i^n$  differ from the expected model images  $\mu_i^n$  due to noise. The object pixels  $x_i$  are reconstructed by minimizing the quadratic function:

$$E = \frac{1}{2} \sum_{n=1}^N \sum_{i=1}^M (d_i^n - \mu_i^n)^2, \quad (3)$$

which is sometimes derived from the log likelihood of the image formation model given the observations in the presence of uniform Gaussian noise. The minimum may be found numerically using a local iterative update algorithm:

$$x_i' = x_i + \beta_x \frac{\partial E}{\partial x_i}, \quad (4)$$

which is the gradient descent update rule with step size  $\beta_x$ . The gradient w.r.t. the object is given by:

$$\frac{\partial E}{\partial x_i} = - \sum_{n=1}^N \sum_{j=1}^M h_{ji}^{em} p_i^n (d_j^n - \mu_j^n) = - \sum_{n=1}^N \sum_{j=1}^M h_{ji}^{em} p_i^n \left( d_j^n - \sum_{k=1}^M h_{jk}^{em} x_k p_k^n \right). \quad (5)$$

The connection to the piFP algorithm becomes clear via the introduction of a set of additional variables – the  $N$  emission intensities for the  $N$  illumination patterns:

$$y_i^n = p_i^n x_i. \quad (6)$$

The update rule for the object (Eq. (4)) can then be split in three consecutive steps with these variables:

$$\text{step 1: } y_i^n = p_i^n x_i \quad (7)$$

$$\text{step 2: } y_i^n = y_i^n + \beta_y \sum_{j=1}^M h_{ji}^{em} \left( d_j^n - \sum_{k=1}^M h_{jk}^{em} y_k^n \right) \quad (8)$$

$$\text{step 3: } x_i' = x_i + \frac{\beta_x}{\beta_y} \sum_{n=1}^N p_i^n (y_i^n - p_i^n x_i) \quad (9)$$

In case the step sizes are chosen to be  $\beta_x = \beta_y = 1$ , Eqs. (7)–(9) constitute the set of updates of the piFP algorithm [18]. It should be noted, however, that in the piFP method the object is updated for each update of the variable  $y_i^n$ , whereas in the optimization of the quadratic function  $E$  the object is updated once after all  $N$  variables  $y_i^n$  have been updated. We have observed that this sequential update of the object in the piFP algorithm results in artefacts in the reconstructed image during the first several iterations, but does not significantly influence the image quality at the convergence point. Moreover, we found that updating an object sequentially may be beneficial for the stability of the piFP algorithm when multi-spot and line illumination patterns are used. Interestingly, Guizar-Sicairos and Fienup have also made a connection to least squares fitting in their treatment of the original ptychographical iterative engine targeting phase retrieval in coherent imaging [30]. They argue that one would expect a more robust algorithm w.r.t noise if all the measurements are used simultaneously when refining the object estimate. We did not observe such an improvement in robustness, which might be explained by the different – incoherent – imaging modality that is considered here.

The key advantage of splitting the optimization of the squared error  $E$  in parts as above is that the update for  $y_i^n$  (step 2), proportional to the gradient, is purely expressed as a convolution. The update for the  $y_i^n$  in Fourier space is then purely local:

$$Y_i^n = Y_i^n + \beta_y \cdot OTF^* \left( D_i^n - Y_i^n \cdot OTF \right), \quad (10)$$

where capital letters indicate the Fourier transform counterparts of the variables,  $OTF$  is the optical transfer function, i.e. the Fourier transform of  $h^{em}$ , and the  $*$  indicates the complex conjugate. The subsequent update for the  $x_i$  is local in direct space to start with.

If the illumination patterns  $p_i^n$  are unknown, they can be reconstructed as well in a similar manner:

$$p_i^n = p_i^n + \beta_p \frac{\partial E}{\partial p_i^n} = p_i^n + \frac{\beta_p}{\beta_y} x_i (y_i^n - p_i^n x_i). \quad (11)$$

Although the recovery of the illumination patterns is not strictly necessary when a DMD is used, it is worth considering for the sake of development of more simple fluorescence microscopes that use *a priori* unknown speckle illumination. In the following set of simulations and reconstructions we have assumed that the illumination patterns at the sample were given by the convolution of the known DMD patterns with the excitation PSF, as in Eq. (2). At the end of our treatment we will shortly revisit the matter of illumination pattern retrieval.

## 2.2 Fourier Ptychography algorithm with Newton-Raphson update

The steepest descent method is often not the most effective way to solve an optimization problem. Methods involving the second order derivative of the objective function, such as the Levenberg-Marquardt (LM) or the Newton-Raphson (NR) algorithms, usually result in faster convergence by tuning the step sizes  $\beta_x$  and  $\beta_y$ . Application of the LM algorithm implies the calculation of the Hessian matrix of the optimized function  $E$  as obtained using Eqs. (2) and (5):

$$L_{ij} = \frac{\partial^2 E}{\partial x_i \partial x_j} = \sum_{n=1}^N \sum_{k=1}^M h_{ki}^{em} h_{kj}^{em} p_i^n p_j^n = \left( \sum_{k=1}^M h_{ki}^{em} h_{kj}^{em} \right) \left( \sum_{l=1}^M \sum_{m=1}^M h_{il}^{ex} h_{jm}^{ex} \left( \sum_{n=1}^N q_l^n q_m^n \right) \right) \quad (12)$$

and multiplication of the gradient of the merit function with the inverse of  $L + \kappa \text{diag}(L)$ , with  $\kappa$  the LM-parameter, rather than with the constant step size  $\beta_x$ . Further simplification is possible if the DMD patterns  $q_i^n$  are designed such that their sums are:

$$\sum_{n=1}^N q_i^n = N \langle q \rangle, \quad (13)$$

$$\sum_{n=1}^N (q_i^n)^2 = N \langle q^2 \rangle, \quad (14)$$

independent of pixel location  $i$ . These conditions can be fulfilled by programming patterns of the DMD in such a way that each DMD pixel is switched “on” the same number of times and, hence, the overall illumination is uniform. In fact, these patterns are preferred over fully randomized patterns, since a uniform total illumination results in a reduced overall noise level. If furthermore we may neglect correlations between the on-off sequences at different DMD pixels then it holds that:

$$\sum_{n=1}^N q_i^n q_m^n \approx N \left( \langle q^2 \rangle - \langle q \rangle^2 \right) \delta_{im} + N \langle q \rangle^2 \quad (15)$$

We are, however, aware that this assumption is only partly correct for our experimental setup. Assuming that the excitation PSF is normalized to unity we then find a Hessian:

$$L_{ij} = N \left( \langle q^2 \rangle - \langle q \rangle^2 \right) \sum_{k=1}^M h_{ki}^{em} h_{kj}^{em} \sum_{l=1}^M h_{li}^{ex} h_{lj}^{ex} + N \langle q \rangle^2 \sum_{k=1}^M h_{ki}^{em} h_{kj}^{em} \quad (16)$$

Application of the LM-algorithm requires the inversion of the matrix  $L + \kappa \text{diag}(L)$ , a daunting task as this is an  $M \times M$  matrix with  $M$  the total number of pixels. This could be done more efficiently by splitting the image in patches but nevertheless requires a substantial numerical effort in matrix inversion. The NR-algorithm, on the other hand, uses only the diagonal part of the Hessian, making the update local again:

$$x_i' = x_i - \frac{1}{L_{ii}} \frac{\partial E}{\partial x_i} \quad (17)$$

with:

$$L_{ii} = N \left( \langle q^2 \rangle - \langle q \rangle^2 \right) \sum_{k=1}^M (h_{ki}^{em})^2 \sum_{l=1}^M (h_{li}^{ex})^2 + N \langle q \rangle^2 \sum_{k=1}^M (h_{ki}^{em})^2. \quad (18)$$

Shift invariance of the illumination and imaging now imply that the sums:

$$K_i^{em} = \sum_{k=1}^M (h_{ki}^{em})^2 = K^{em}, \quad (19)$$

$$K_i^{ex} = \sum_{l=1}^M (h_{li}^{ex})^2 = K^{ex}, \quad (20)$$

are also independent of pixel location. Then the diagonal part of the Hessian is simply proportional to the identity matrix:

$$L_{ii} = N \left( \langle q^2 \rangle - \langle q \rangle^2 \right) K^{em} K^{ex} + N \langle q \rangle^2 K^{em}, \quad (21)$$

for all pixels  $i$ . The crucial approximation in deriving this result is the neglect of the correlations between the on-off sequences of the different DMD pixels. We will apply the NR-algorithm under this approximation in the following.

### 3. Simulations

#### 3.1 Simulation setup

The original piFP algorithm was compared to the piFP algorithm with Newton-Rapson (NR) update step size in simulations. The performance of both image reconstruction algorithms was evaluated for various types of illumination patterns. A simulated resolution target, shown in Fig. 1(a), was used as test object. The imaging system was described by the scalar diffraction based Airy PSF with full width at half maximum  $FWHM \approx 0.513 \lambda_{em}/NA$ , where  $\lambda_{em} = 530$  nm is the emission wavelength and  $NA = 1.4$  is the numerical aperture of the objective. A pixel of the simulated resolution target in the sample plane equals  $\lambda_{em}/16NA$  and the numbers of line groups in Fig. 1(a) indicate the pitch of the group in units of  $\lambda_{em}/8NA$ . Hence, group 4 is at the limit of the widefield imaging and group 2 is at the limit of the structured illumination imaging.

We have tested three types of DMD patterns: multi-spot, pseudo-random and line patterns, as shown in Figs. 1(b)-1(d). A multi-spot DMD pattern is generated as a square grid of spots with the size of one pixel. The pattern is then translated  $N-1$  times by one pixel in order to illuminate the whole object. Pseudo-random DMD patterns are generated in the following way. Suppose we have a set of  $N$  pseudo-random DMD patterns. Each pixel is switched “on”  $S$  times making the sum of the  $N$  patterns uniform. The  $S$  patterns for which any pixel is non-zero are randomly drawn from the total set of  $N$  patterns. In this way we can generate pseudo-random patterns with controlled sparsity and uniform total illumination. Finally, several shifts and rotations of a binary line grid are used to generate a set of line patterns. The maximum frequency of the projected patterns is limited to  $f_{cutoff} = 2NA/\lambda_{ex}$  in an epi-fluorescence microscope setup. Hence, assuming totally incoherent DMD illumination, the generated illumination patterns are multiplied in the Fourier domain by the incoherent OTF of the optical system with a cutoff frequency  $f_{cutoff}$  in order to obtain the set of illumination patterns  $p_i^n$  in the sample plane. The  $N$  illumination patterns  $p_i^n$  are made to be uniform in their sum and the total intensity of  $N$  images  $d_i^n$  is taken equal for all the described pattern types. The illumination intensity per pixel summed over all patterns is set to  $2.5 \times 10^4$  photons and Poisson noise is added to each simulated image. Although the quadratic error metric of Eq. (3) does not apply to Poisson noise, it nevertheless can be expected to minimize the misfit between the noisy observations and expected images based on the image formation model. The described image reconstruction algorithms were implemented in MATLAB (Mathworks, USA) using the DIPImage toolbox [31]. The reconstructions were carried out according to Eqs. (7)–(9), where an object with uniform intensity was used as an initial guess for the object variables  $x_i$  considered here.

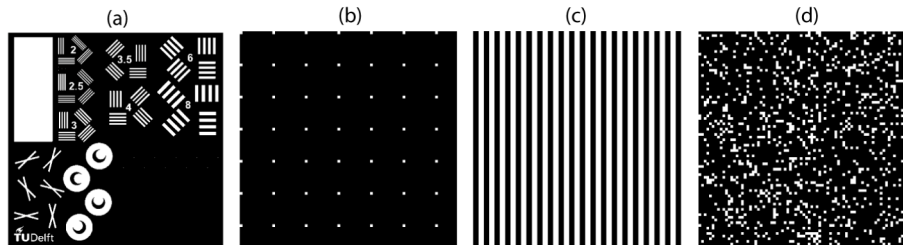


Fig. 1. (a) Simulated resolution target. Line group 4 has the pitch of  $\lambda_{em}/2NA$ , corresponding to the limit of the widefield imaging. (b)-(d) Examples of illumination patterns generated at the DMD: multi-spot (b), line (c) and pseudo-random (d) patterns.

### 3.2 Stopping criterion

We have shown that the piFP-algorithm is equivalent to least squares optimization, which is known to be an ill-posed mathematical problem in the absence of regularization. We have indeed observed that letting the iteration run to reach the best possible numerical convergence tends to lead to undesirable graininess in the reconstruction, i.e. to noise amplification. This effect becomes apparent when examining the development of the modulation transfer function (MTF) with iterations (Fig. 2). In order to obtain the MTF curves we have simulated piFP imaging of a line object with a thickness of one pixel. The MTF was calculated as the Fourier transform of the line profile in the reconstructed image at each iteration of the piFP algorithm. As seen in Fig. 2, with the growing number of iterations the high frequency components are increasingly amplified, which simultaneously leads to the noise amplification. In addition, with the growing number of iterations the shape of the MTF curve becomes increasingly less smooth, causing ringing artefacts in the reconstructed image.

Clearly, some form of regularization is needed in order to prevent this problematic noise blowup and avoid ringing artefacts. We have found that abandoning numerical precision as criterion for terminating the iteration in favour of a more loose criterion on the error metric  $E$  defined in Eq. (3) can effectively serve as regularization for the optimization problem. It appears that  $E$  converges to a value following from the noise statistics only. In case there is only shot noise, this limiting value, which we term noise level  $NL$ , is:

$$NL = \sum_{n=1}^N \sum_{i=1}^M d_i^n. \quad (22)$$

We obtained satisfactory reconstructions when the iterative optimization was stopped if the error  $E$  is equal to  $NL$  or within a small fraction of it, say within 1%. This convergence criterion is reached within 3-60 iterations (we consider  $N$  updates of the object for  $N$  illumination patterns to be one iteration of the piFP algorithm), depending on the type of projected patterns and the choice of  $\beta$ .

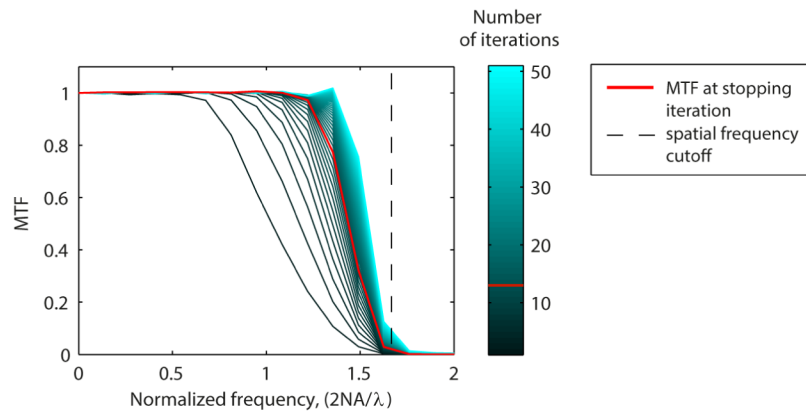


Fig. 2. Change of the MTF curves during the piFP iterations. Multi-spot illumination patterns with a pitch of 12 pixels, which corresponds to a spatial frequency cutoff of 1.7 times the widefield bandwidth  $2NA/\lambda$ , were used to simulate the illumination of a line object. The MTF is calculated as the Fourier transform of the line profile at each iteration of the piFP reconstruction algorithm. The stopping iteration is highlighted in red. The vertical dashed line indicates the highest possible resolution improvement estimated from the pitch of the projected illumination patterns.

### 3.3. The effect of sparsity and number of pseudo-random patterns

Figure 3 shows a comparison of the image quality for pseudo-random patterns with different sparsity. The fill factor  $f$  – the percentage of non-zero DMD pixels per pattern – is the measure of sparsity of the projected patterns. Here we used a total number of illuminations  $N$

= 144 and the original piFP reconstruction algorithm [18]. The illumination dose is rescaled in order to keep the total illumination intensity of  $N$  images constant regardless of the sparsity. Figure 3(a) shows the relative difference between the error, calculated according to Eq. (3) and the noise level, calculated according to Eq. (22). The crossings of the curves with the horizontal dashed line indicate when the error reaches the noise level within 1%, the stopping condition for the iterative algorithm. A comparison of the signal-to-noise ratios (SNR) is given in Fig. 3(b). The SNR was measured as the mean signal of the uniform rectangle in the top-left corner of the resolution target divided by the standard deviation of the signal across that uniform area (background is zero). The horizontal dashed line shows the SNR in a uniformly illuminated widefield image with the same illumination dose as the cumulative dose of the  $N$  pseudo-random patterns. Figure 3(c) shows the resolution improvement as a function of the number of iterations. The full width at half maximum (FWHM) was estimated by fitting a Gaussian function to point objects in the reconstructed images of the resolution target (not visible in Fig. 1(a)). The horizontal dashed line shows the FWHM of a widefield image.

The simulation results indicate that patterns with high fill factor, which imitate speckle illumination, are inferior to patterns with lower fill factor in terms of resolution improvement and noise suppression. However, the improvement in FWHM and SNR for lower fill factor comes at the expense of a reduced convergence speed. For the given number of illumination patterns  $N = 144$ , one iteration takes 2.2 seconds on an Intel Xeon E5-1620 v2 CPU with 3.70 GHz clock speed. Hence, the total reconstruction time increases from 6.6 seconds in case  $f = 20\%$  to 2.2 minutes in case  $f = 0.7\%$ . Moreover, in order to obtain even lower sparsity, one has to increase the total number of illumination patterns, which will lead to further deceleration of the reconstruction process. In this sense, confocal imaging can be seen as a particular case of structured illumination, in which the lowest possible sparsity is achieved.

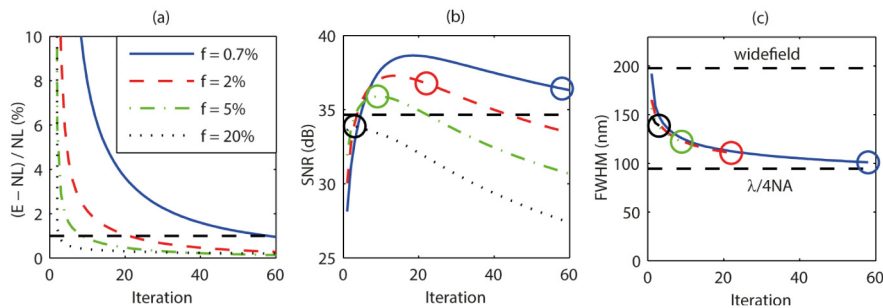


Fig. 3. Comparison of the image quality for pseudo-random patterns with different sparsity. (a) Illustration of the stopping condition. The crossings of the curves with the horizontal dashed line indicate when the error reaches the noise level within 1%. (b) Lower fill factor results in higher SNR. Horizontal dashed line shows the SNR in a widefield image. Round markers indicate the final iteration according to our stopping criterion. (c) Lower fill factor results in smaller FWHM. The dashed lines show the FWHM in a widefield image and the best possible resolution  $\lambda/4NA$ .

Another parameter influencing the quality of the reconstructed image in the case of pseudo-random illumination is the total number of illumination patterns  $N$ . Figure 4 shows that the resolution improves with increasing number of illumination patterns, probably because cross-talk effects from neighboring pixels are averaged out over multiple acquisitions. This differs from the situation with spatially periodic illumination, where the number of projected patterns plays a secondary role. When line or multi-spot illumination patterns are used, the resolution of the reconstructed image mainly depends on the spatial frequency content (pitch) of the projected illumination patterns.

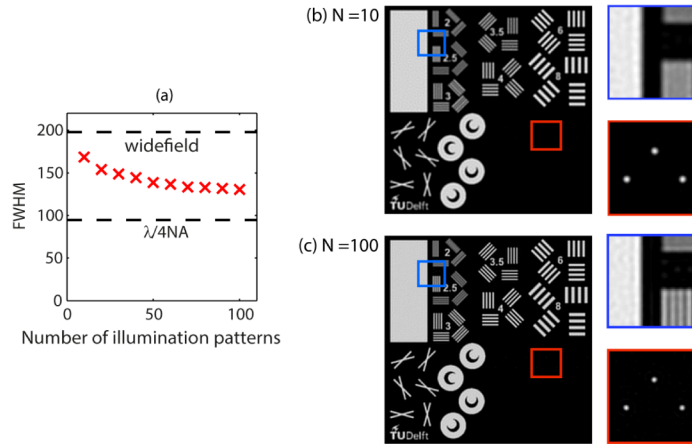


Fig. 4. (a) In the case of pseudo-random illumination, the resolution of the reconstructed image improves with increasing number of illumination patterns  $N$ . We used 10 illumination patterns in (b) and 100 illumination patterns in (c). The sparsity of the patterns is kept constant ( $f = 10\%$ ).

### 3.4. Comparison of illumination pattern types

Theoretically, projecting a line or a multi-spot pattern with a spatial frequency as large as  $2NA/\lambda_{ex}$  will result in the largest resolution improvement. However, due to the low modulation at the limit of the OTF in an incoherent illumination system and the presence of noise, a 10-30% smaller spatial frequency of the projected pattern is used in real imaging systems. We used a pitch of 12 pixels (12 pixels =  $1.5 \times \lambda_{ex}/2NA$ ) for the multi-spot and line patterns and a sparsity of 0.7%, which results in an average distance of 12 pixels, for the pseudo-random patterns. These values for the pitch and the average distance correspond to a spatial frequency of the projected patterns that is 33% smaller than the cutoff frequency of the microscope. The total number of illuminations is kept at  $N = 144$  for each pattern type, while keeping the total illumination dose constant. Since within a single piFP iteration the object is updated  $N$  times, the same number of illuminations for each pattern type is required in order to provide a fair comparison of the convergence speeds of the algorithm for different types of illumination patterns. The required number of line pattern illuminations was obtained by using 12 shifts and 12 rotations of the line grid. This is different from standard SIM acquisitions in which 3 to 5 shifts and 3 or 5 rotations are used.

The comparison of the performance of the two described algorithms and three types of illumination patterns is given in Fig. 5. The convergence speed is significantly higher when multi-spot and line patterns are used instead of pseudo-random illumination patterns. Furthermore, as predicted by theory, the convergence speed of the piFP algorithm with NR update rule is improved in comparison to the original piFP algorithm for all types of illumination patterns. The effect is most evident in the case of pseudo-random patterns, where the number of iterations is reduced by a factor of two; for the multi-spot and line patterns the improvement is inessential. Furthermore, we observe that application of the NR update rule leads to a moderately reduced SNR and slightly improved FWHM at the stopping point of the iteration. In the case of pseudo-random illumination patterns the decrease in SNR and FWHM when NR update rule is used is negligible. In the case of multi-spot and line illumination patterns the SNR decrease is within 15% and the FWHM improvement is within 10%. This result reflects the trade-off between resolution improvement and noise amplification – sharper images typically exhibit more pronounced noise structures in the uniform areas.

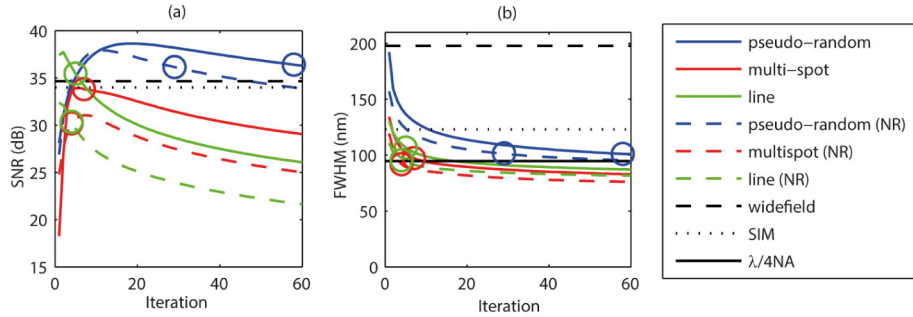


Fig. 5. Performance of the original piFP algorithm compared to the performance of the piFP algorithm with NR update rule for different types of illumination patterns. SNR (a) and FWHM (b) curves display the trade-off between the sharpness of the structures and the noise appearance in the reconstructed images. Application of the NR update rule leads to faster convergence, reduced SNR and improved FWHM. Round markers indicate the final iteration according to our stopping criterion. The SNR and FWHM values of the widefield and conventional SIM images are given for comparison.

The SNR and FWHM values of a conventional SIM image, reconstructed from 9 line grid illuminations using the generalized Wiener filter reconstruction [32], are given for comparison. It should be noted, that the illumination patterns do not reach maximum modulation, since they are projected from the DMD onto the sample fully incoherently via the objective lens, and are hence blurred by the illumination PSF. The modulation depth of the projected pattern is an important parameter, influencing the quality of the SIM image. A conventional SIM image reconstructed from acquisitions with larger modulation of the illumination pattern at the sample would have resulted in a smaller FWHM. Achieving improved modulation in DMD-generated illumination patterns is in principle possible by treating the DMD as a diffraction grating and filtering out the DC component in the Fourier plane. Another option would be to exploit the flexibility of the DMD to study the formation of three-dimensional illumination patterns.

Finally, reconstruction with the piFP algorithm and the proposed stopping criterion is independent of the underlying sample structure and applied illumination type. In contrast to the generalized Wiener filter reconstruction, where the regularization parameter has to be set empirically, the proposed method does not require adjustment of parameters with unclear impact on the final image quality. The novel stopping criterion we propose automatically provides for the needed regularization.

## 4. Experiment

### 4.1. Experimental setup

We conducted a series of experiments in order to test the performance of the modified piFP algorithm with the different illumination pattern types. Our DMD-based microscope is built by complementing an inverted Olympus IX71 fluorescence microscope with an illumination branch that provides the projection of the DMD patterns onto the sample. An expanded and despeckled beam of a 488 nm laser is used to illuminate the DMD. The DMD pixels with physical size of 13.68  $\mu\text{m}$  are then demagnified to 137 nm in the sample plane with the help of a 250:150 mm lens relay and a  $60\times/0.7$  air objective (Fig. 6). Although higher resolution images can be produced with immersion objectives, this is not needed for the current comparison study. The actually measured NA of the excitation beam in the back focal plane of the objective lens amounts to 0.6, thus, illumination and detection NA slightly differ. The pixel sampling of the Orca Flash 4.0 camera corresponded to 108 nm at the sample, which provides slight undersampling ( $\sim 10\%$ ) of the specimen compared to the maximum cutoff  $2NA_{\text{im}}/\lambda_{\text{em}} + 2NA_{\text{il}}/\lambda_{\text{ex}}$ . A precise mapping of the DMD to the camera is required for accurate prediction of the illumination patterns from the patterns displayed on the DMD. We have used an earlier developed calibration procedure in order to establish the correspondence between

each DMD pixel and its image on the camera. The details on the optical design of the setup and the calibration procedure are given in [33].

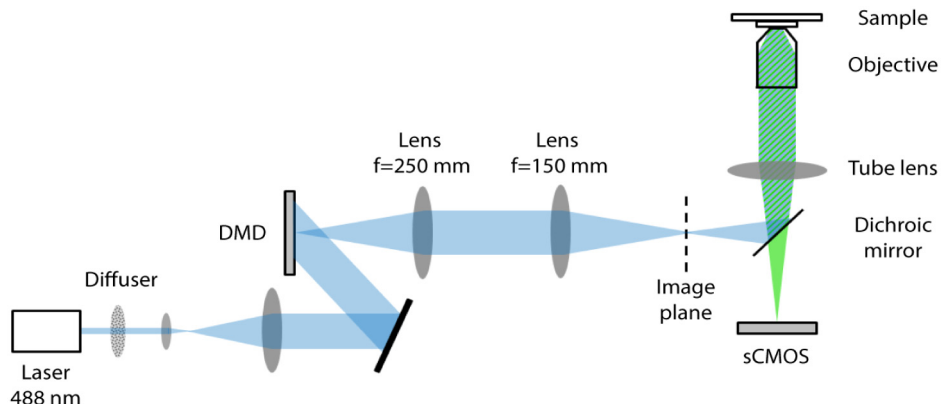


Fig. 6. Schematic view of the DMD-based fluorescence microscope. The beam of the 488 nm diode laser is despeckled and expanded in order to provide illumination of the DMD surface. The DMD patterns, demagnified by the 250:150 mm optical relay and by the objective lens, are projected onto the sample. The sCMOS camera detects fluorescence from the sample. One camera frame is taken for each illumination pattern [33].

#### 4.2. Imaging fluorescent beads

Multi-spot and pseudo-random illumination patterns were applied to a sample containing 100 nm diameter fluorescent microspheres (Invitrogen, CA, USA) deposited on a microscope coverslip. We have used a pitch of 10 DMD pixels for the multi-spot illumination patterns and a fill-factor of 1% and 10% for the pseudo-random illumination patterns. The total number of illuminations is  $N = 100$  and the overall illumination dose is kept the same for all illumination types by adjusting the power of the laser.

The original piFP algorithm assumes reconstruction of 2D slices and does not take the background and the out-of-focus light into account. The background intensity is, however, always present in the acquired images. We found that the reconstruction can be improved by adding a background to the estimates of the emission intensities in step 1 of the algorithm. This background was estimated as the 20th percentile of the intensity in the set of  $N$  collected images. The expected noise level  $NL$  was estimated from the read-out noise of the camera and the Poisson statistics of light. The stopping criterion proposed in section 3.2 was reached within 8 iterations in case of the multi-spot illumination patterns. However, in case of the pseudo-random patterns the predicted noise level does not correspond to the convergence value of the error metric  $E$ . We assume that an additional noise source is present in the images acquired under pseudo-random illumination that hinders the correct noise level estimation in this case. Low fill factors lead to high additional noise, while high fill factors provide some averaging of the background intensity and lead to lower noise. Therefore, an alternative stopping criterion was used for pseudo-random illumination patterns: the convergence is reached when the change of  $E$  between two consecutive iterations is within a small fraction (we have taken 2%) of  $E$ . This criterion is reached for  $f = 1\%$  and  $f = 10\%$  within 17 and 4 iterations respectively.

The comparison of the images, acquired for the various illumination pattern types and reconstructed by the original piFP algorithm, is given in Fig. 7. The zoom-in area shows neighboring beads, which are not resolved in a widefield image (Fig. 7(a)), but are clearly resolved in the reconstructed image after multi-spot illumination (Fig. 7(c)). The resolution is also better than obtained from a standard Richardson-Lucy deconvolution of the widefield image (Fig. 7(b)). We observe that the relative intensities of the fluorescent beads are not preserved in the image reconstructed after the pseudo-random illumination patterns with low

fill factor (Fig. 7(d)). This qualitative observation indicates that the pseudo-random illumination patterns with low fill factor, which would theoretically lead to higher resolution improvement than the patterns with high fill factor, cannot be reliably applied in practice. The piFP reconstruction after pseudo-random illumination patterns with higher fill factor displays correct relative intensities of the beads (Fig. 7(e)); however, as predicted by the theory, it shows weaker resolution improvement compared to the piFP reconstruction after the multi-spot illumination patterns.

We have observed that in case of multi-spot patterns and pseudo-random patterns with high fill factor, the piFP algorithm with NR update rule is only marginally faster than the original piFP algorithm; at the same time, it is less stable and occasionally leads to diverging solutions when applied to experimental data. Hence, for most practical cases in fluorescence microscopy the original piFP algorithm converges sufficiently fast and is preferred because of its stability. The NR update rule in piFP algorithm can be recommended when a large number of sparse pseudo-random illumination patterns is used.

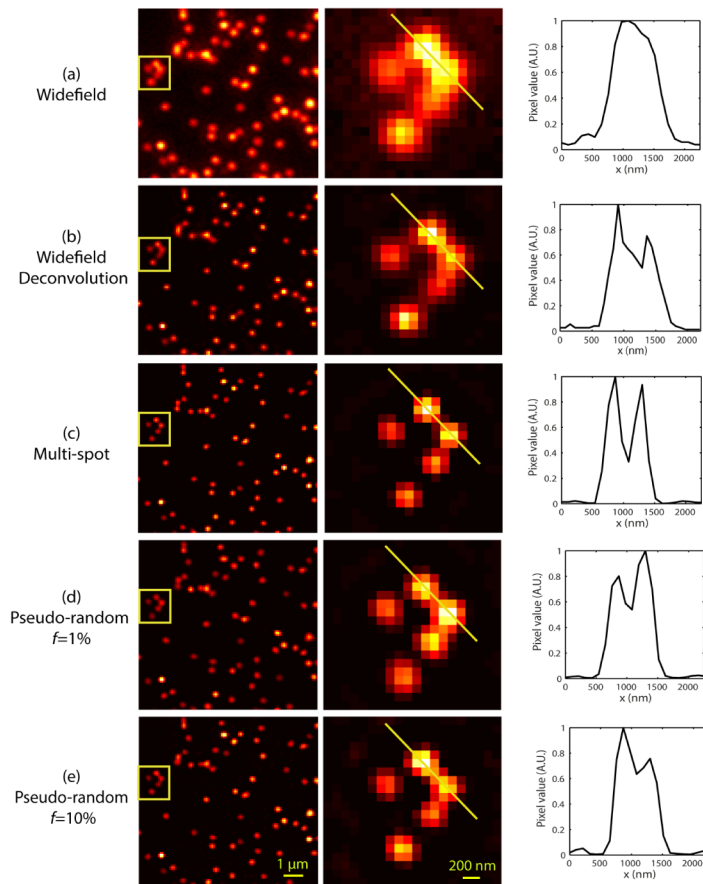


Fig. 7. Comparison of piFP reconstructions for different illumination patterns. The sample containing 100 nm diameter fluorescent microspheres was imaged using a  $60 \times /0.7$  air objective. (a) Widefield image. The two neighboring beads shown in the zoom-in area are not resolved. (b) Widefield image deconvolved using the Richardson-Lucy algorithm shows slight resolution improvement. (c) piFP reconstruction for the multi-spot illumination patterns. The two neighboring beads are well resolved. (d) piFP reconstruction for the pseudo-random illumination patterns with fill factor  $f = 1\%$ . The neighboring beads are separated, however, the relative intensities of the beads are not preserved. (e) piFP reconstruction for the pseudo-random illumination patterns with fill factor  $f = 10\%$  shows weaker resolution improvement compared to the multi-spot patterns.

### 4.3. Imaging filamentous samples

The same multi-spot and pseudo-random patterns as described in section 4.2 were tested on a test slide with bovine pulmonary artery endothelial (BPAE) cells (Invitrogen, CA, USA), in which F-actin is stained with Alexa Fluor 488 phalloidin. Estimation of the noise level is a demanding task for this sample, since its three-dimensional structure leads to high background and out-of-focus light. Therefore, we have used the stopping criterion based on the change of  $E$  between two consecutive iterations as described in section 4.2. In agreement with the results achieved on the bead sample, multi-spot illumination patterns produce the most visually satisfactory reconstruction (Fig. 8(d)), while pseudo-random patterns with 1% fill factor result in enhanced graininess in the reconstructed image (Fig. 8(e)). As can be seen in Fig. 7(d), this graininess leads to inaccurate representation of the relative intensities in the image. Finally, an image reconstructed for pseudo-random illumination patterns with 10% fill factor displays pronounced low frequency noise structures that are typical for SIM images reconstructed with insufficient apodization [34] (Fig. 8(f)).

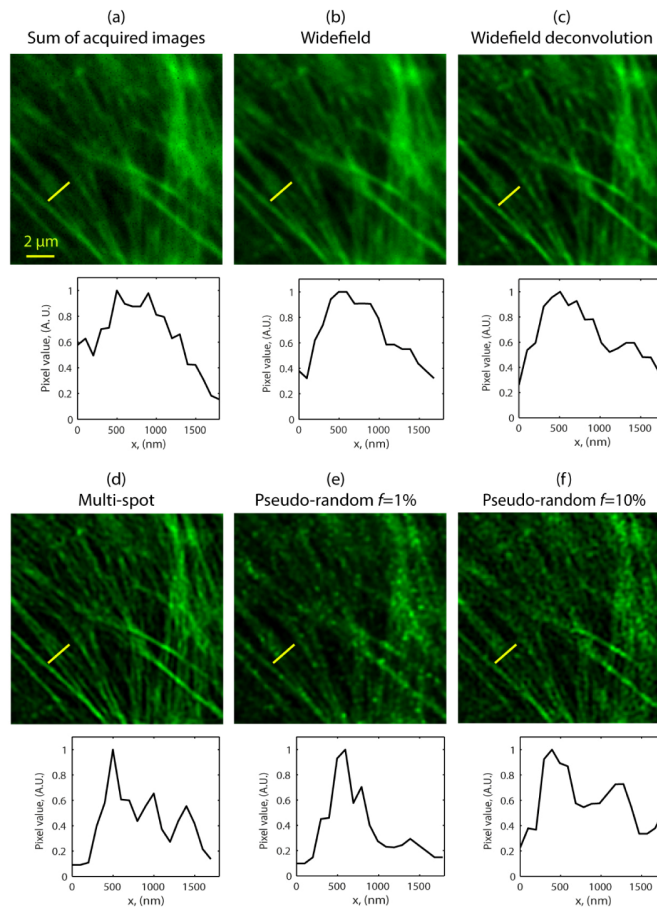


Fig. 8. Comparison of piFP reconstructions for different illumination patterns. Images of the BPAE cells were acquired using a  $60 \times /0.7$  air objective. (a) The sum of all acquired frames is given to demonstrate the uniformity of the illumination. (b) Widefield image. (c) Deconvolution of the widefield image using Richardson-Lucy algorithm. (d) piFP reconstruction for the multi-spot illumination patterns. (e) piFP reconstruction for the pseudo-random illumination patterns with fill factor  $f = 1\%$  showing enhanced graininess. (f) piFP reconstruction for the pseudo-random illumination patterns with fill factor  $f = 10\%$  showing pronounced low frequent noise structures. The profile plots along the highlighted yellow line only show three distinct filaments for the multi-spot reconstruction in (d).

#### 4.4. Reconstruction of illumination patterns

An obvious advantage of using a DMD compared to speckle illumination is having *a priori* knowledge about the projected illumination patterns, which significantly simplifies the reconstruction process in terms of speed and robustness. In the above we did not include the reconstruction of the illumination patterns  $p^n$  in the algorithm, since we use pre-designed patterns generated by the DMD and assume that these illumination patterns are mapped to the camera pixel grid with high accuracy. We have added the illumination pattern reconstruction step according to Eq. (11) in order to test the influence of this additional step in the algorithm on the final reconstruction. We have used  $N$  different illumination patterns, in contrast to the original piFP algorithm [18], where  $N$  shifts of a single DMD pattern are used. Hence, in our method each of the  $N$  illumination patterns has to be reconstructed separately. The initial estimate of each illumination pattern  $p^n$  is given by the expected illumination pattern, i.e. by the known DMD pattern blurred by the excitation PSF of the objective. As shown in Figs. 9(a) and 9(b), the algorithms with and without the  $p^n$  refinement step produce comparable sample reconstructions; however, the algorithm with the  $p^n$  refinement step takes several iterations longer to reach convergence. Reconstructed illumination patterns match the expected illumination patterns well, thereby confirming the high accuracy of the used calibration procedure.

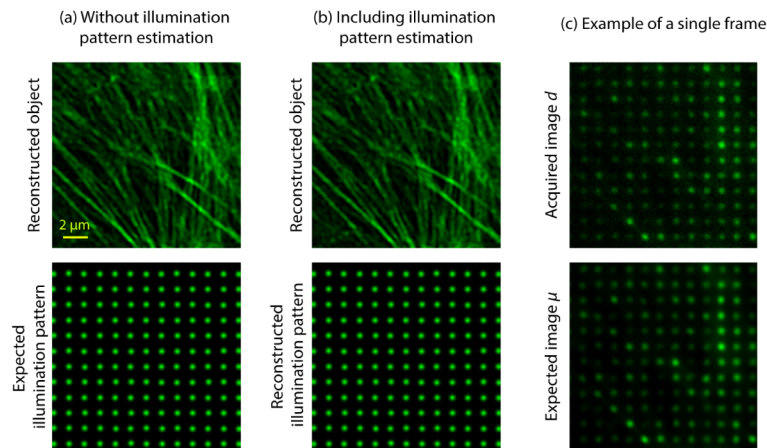


Fig. 9. The algorithms with and without the reconstruction of the illumination patterns produce comparable results. (a) piFP reconstruction using known illumination patterns reaches convergence in 7 iterations. Images show the reconstructed object and an example of the known illumination pattern. (b) piFP reconstruction with estimation of the illumination patterns reaches convergence within 9 iterations. Images show the reconstructed object and an example of the estimated illumination pattern. (c) An example of the actually measured image  $d^n$  and the corresponding expected image  $\mu^n$  in case the known illumination patterns are used.

We have also implemented an illumination pattern reconstruction taking the uniform sum illumination constraint of Eq. (13) into account using a Lagrange multiplier approach. This procedure gave rise to a similar outcome. It is necessary in the pattern estimation to use the prior knowledge of the DMD-patterns as starting point for the iteration in order to guarantee convergence. Taking uniform illumination patterns as starting point did not result in reasonable reconstructions. We may conclude that the piFP algorithm can work as a “semi-blind SIM” deconvolution, in contrast to the fully “blind SIM” deconvolution approach [13,14]. A comparison of the actually measured image  $d^n$  and the corresponding expected image  $\mu^n$  is given for illustration in Fig. 9(c).

In order to further test the strength of the prior knowledge of the illumination patterns we have also compared the expected and reconstructed pseudo-random illumination patterns with higher fill-factor ( $f = 10\%$ ). Figure 10 gives the representation of the difference between the

reconstructed and expected illumination patterns and reveals good correspondence between the two with errors typically below 10%.

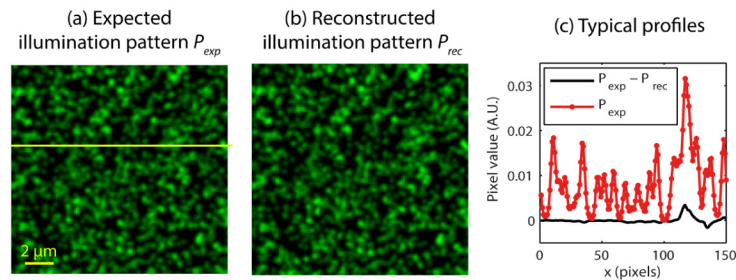


Fig. 10. Comparison of the expected (a) and reconstructed (b) patterns in case of pseudo-random illumination with fill-factor  $f = 10\%$ . (c) The profile of the difference  $P_{exp} - P_{rec}$  along the yellow line shown in (a) reveals good correspondence between the expected and reconstructed illumination patterns.

## 5. Conclusion

In this paper we have shown that the piFP algorithm, which is the FP concept applied to fluorescence microscopy, can be interpreted as a steepest descent optimization of a quadratic function. This representation opens opportunities to modify, improve or specifically tailor the piFP algorithm to the details of the given optimization problem. We have demonstrated in simulations the improvement of the convergence speed of the piFP algorithm by modifying its update coefficients according to the Newton-Raphson rule.

We have used a DMD-based fluorescence microscope with widefield detection and image reconstruction with the piFP algorithm to test various illumination patterns for resolution improvement and noise enhancement in fluorescence microscopy. We also show that accurate calibration of the microscope enables one to omit the step of reconstructing the illumination patterns in the algorithm. We demonstrate, both in simulations and in experiments, that the illumination patterns with a regular spatial structure, such as multi-spot or line patterns, are preferred over randomized patterns even when the illumination patterns are known. Irregular illumination patterns do not have a sharply peaked spatial frequency content but instead a more smeared out spectrum. The reconstructed MTF in the region beyond the widefield cutoff can therefore be anticipated to be lower than for regular illumination patterns. In order to achieve the same sharpness this will come at the expense of significant noise enhancement.

According to our simulations, pseudo-random patterns with high sparsity provide better resolution improvement and noise suppression than pseudo-random patterns with low sparsity. However, in practice, there appears to be an additional noise source present in the images reconstructed from pseudo-random illuminations. This noise source plays a larger role in case the sparsity of the pseudo-random illumination patterns is high, resulting in grainy images. Tracking the root cause of this effect is the target of follow-up research. We speculate here that it may lie in imperfections of the imaging model. First of all, our two-dimensional imaging model does not take the three-dimensional structure of real samples and of the microscope PSF into account. Second, the scalar diffraction based Airy PSF model is a simplification at the moderately high  $\text{NA} = 0.7$  at which the images were acquired. Finally, slight non-uniformities and correlations in the illumination patterns due to insufficiently suppressed spatial coherence in the illumination may also play a role. Extending the piFP method to incorporate these effects is an important next step in developing the piFP imaging technique. Regularization techniques may also be added into the mix to establish a form of noise suppression. Finally, an in-depth comparison of the piFP method with other reconstruction methods, notably the joint Richardson-Lucy deconvolution method [35,36], would further serve to benchmark the algorithm.

## **Acknowledgments**

We would like to thank Guoan Zheng for kindly providing the original software for the piFP algorithm for comparison purposes, and Erik Manders and Ronald Breedijk for fruitful discussions. This research is supported by the Dutch Technology Foundation STW (<http://www.stw.nl/>), which is part of the Netherlands Organization for Scientific Research (NWO), which is partly funded by the Ministry of Economic Affairs, Agriculture and Innovation.